# Nonlinear operation of resonant sensors based on weakly-coupled resonators: experimental investigation of an actively-coupled architecture

Jérôme Juillard, Ali Mostafa, Pietro Maris Ferreira

# Nonlinear operation of resonant sensors based on weakly-coupled resonators: experimental investigation of an actively-coupled architecture

Jérôme Juillard, Ali Mostafa, Pietro Maris Ferreira

**Abstract - This paper is aimed at the validation of a theoretical analysis of the properties of nonlinearly-operated weakly-coupled resonators (WCRs) for resonant sensing applications. In particular, we investigate the relationships between the operating point of such devices and different performance indicators, such as parametric sensitivity, sensitivity to drive level and to noise, and bandwidth. To this end, a couple of high-Q MEMS resonators exhibiting nonlinear restoring and damping forces are used. A careful characterization of the resonators and their associated electronics is made, resulting in a very good, quantitative fit between the experimental results and those predicted by theory.**

# I Introduction

Because of their large parametric sensitivity and their capacity to reject environmental drift, sensor architectures based on actively- and passively-coupled MEMS resonators are a subject of current research interest [1-4]. While the linear theory of operation of such devices is well-known [5-6], there is little theoretical background concerning their nonlinear (large oscillation amplitude) operation. However, some recent studies show there may be a practical interest to operating in such a regime, demonstrating, on a case-by-case basis, improvement in measurement range [7], signal-to-noise ratio [8], or drive voltage fluctuations [9] for example.

In [10], we have presented a comprehensive theoretical framework for modeling WCRs subject to nonlinear restoring forces, as well as nonlinear damping forces. Based on our analysis, some common characteristics of nonlinear WCRs could be established. These properties are summed up in Appendix A of this paper. In this work, we aim at illustrating and commenting these properties in the context of an experimental study, far from the ideal framework of [10]. It should be stressed that we do not seek to demonstrate a hypothetical improvement in performance compared to "conventional" frequency-modulated resonant sensors, but merely to validate our theoretical analysis, provide some helpful examples and gain some critical insight.

To this end, a discrete PCB implementation of the actively-coupled architecture shown in Fig. 1 is used: it is a mutually injection-locked oscillator (MILO) consisting of two MEMS resonators, an analog front-end (AFE), and a digital mixer ensuring the active coupling of the resonators, as studied in [7]. The circuit and the MEMS resonators are described in detail in section II. In particular, the nonlinear characteristics of the resonators are established, and the connection between electrical measurements and

theoretical framework is made. Section III is dedicated to an experimental sensitivity analysis of the system, aimed at validating the quasi-static properties of nonlinear WCRs established in [10] (and recapitulated in appendix A). Section IV is focused on the spectral analysis of the measured signals and illustrates the amplitude-dependent finite bandwidth of these systems. Section V is dedicated to a discussion and some concluding remarks.

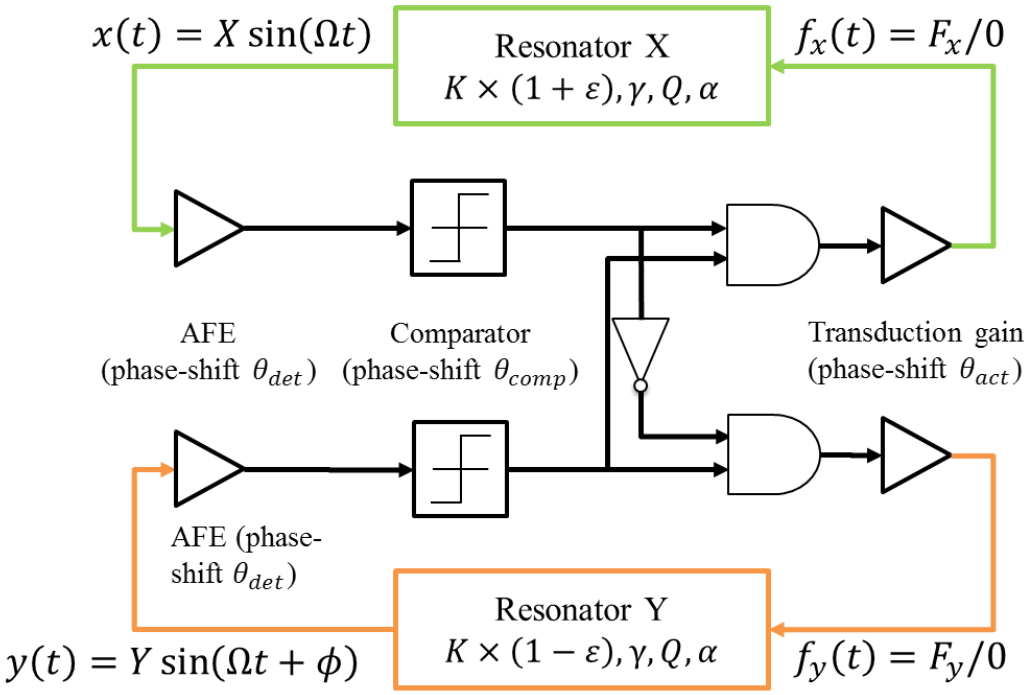


Fig. 1 – System-level view of a MILO based on a digital mixer.

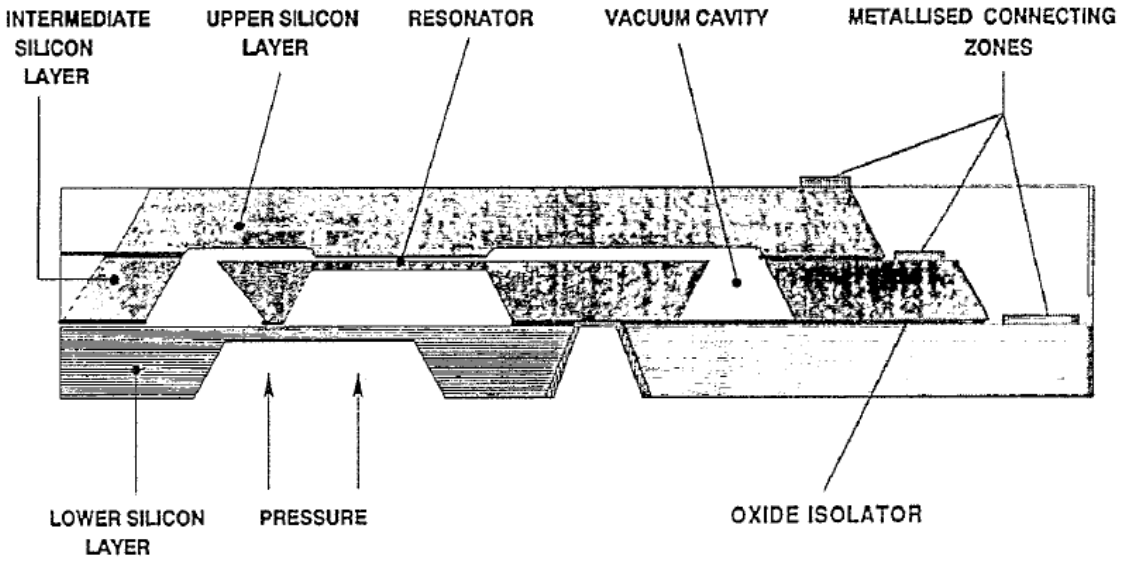


Fig. 2 – Resonator mechanical structure (from [11]). The resonator is modeled as a clamped-clamped beam with an imperfect clamping condition (at the left end) preventing nonlinear hardening [12].

# II Description of the setup[1]

## *II-1 MEMS resonators*

The MEMS resonators used in these experiments are two vacuum-packaged resonant gauges taken from P90 pressure sensors, presented in [11] and characterized in detail in [12-13]. These one-port resonators, shown in Fig. 2, consist in an electrostatically-actuated and capacitively-detected silicon beam, with natural frequency $f_0 \approx 69$kHz and quality factor $Q \approx 2 \times 10^4$. One end of the beam is perfectly clamped while the other is attached to the membrane used as a pressure sensing element. As a consequence of this imperfect clamping condition, no stress-stiffening is observed in the gauges, even at very large oscillation amplitudes [12], electrostatic softening being the dominant source of nonlinearity as far as nonlinear restoring forces are concerned. As reported in [14], internal resonances also occur in these resonators outside of their nominal operating range, resulting in an apparent decrease of their quality factor. This may adequately be modelled as a nonlinear damping phenomenon, as shown in section II-3.

### II-1-a Simplified model of the resonators

Each resonator is accurately described by a single-DOF non-dimensional model resulting from the Galerkin projection of the electrostatically-actuated Euler-Bernoulli beam equation on the first clamped-clamped beam eigenmode [15]:

$$(1+\kappa)x + \left(\frac{1}{Q_x} + \alpha_x x^2\right)\frac{dx}{dt} + \frac{d^2x}{dt^2} = \eta_x \frac{\left(1+v_x(t)\right)^2}{(1-x)^{3/2}} + n_x(t), \qquad \text{(1-a)}$$

$$(1-\kappa)y + \left(\frac{1}{Q_y} + \alpha_y y^2\right)\frac{dy}{dt} + \frac{d^2y}{dt^2} = \eta_y \frac{\left(1+v_y(t)\right)^2}{(1-y)^{3/2}} + n_y(t), \qquad \text{(1-b)}$$

where $x$ or $y$ designates the relative displacement of the center of the beam with respect to the electrostatic gap, $\kappa$ is a parameter representing the mechanical detuning of the resonators with respect to their average unbiased natural frequency, $\eta_x$ and $\eta_y$ are electromechanical transduction coefficients (see below), $n_x(t)$ and $n_y(t)$ are independent random forces acting on the resonators, and $v_x \ll 1$ (resp. $v_y$) is the ratio of the drive voltage $v_{DRVx}(t)$ (resp. $v_{DRVy}(t)$) of the resonator to its DC bias voltage $V_{Bx}$ (resp. $V_{By}$). For a clamped-clamped beam resonator, static pull-in occurs at 40% of the gap, as a static analysis of (1) shows. The expression of the electromechanical coefficient is then simply:

$$\eta = \frac{2}{5}\left(\frac{3}{5}\right)^{3/2} \times \left(\frac{V_B}{V_{PI}}\right)^2 \approx 0.186 \times \left(\frac{V_B}{V_{PI}}\right)^2, \qquad (2)$$

where $V_{PI}$ is the value of the pull-in voltage of the resonator.

[1] Note that, in the experiments of sections II, III and IV, no particular precaution is taken to control temperature, ambient pressure or other environmental factors.

| Symbol | Meaning | Unit | Symbol | Meaning | Unit |
|---|---|---|---|---|---|
| $x, y$ | Displacement of resonators | ND | $X, Y$ | Mechanical amplitudes of resonators | ND |
| $R$ | Ratio of mechanical amplitudes | ND | $\phi$ | Phase difference of resonators | (°) |
| $Q$ | Quality factor | ND | $\alpha$ | Nonlinear damping coefficient | ND |
| $\eta$ | Electromechanical coefficient | ND | $V_{PI}$ | Static pull-in voltage | (V) |
| $\kappa$ | Relative stiffness mismatch (mech. only). | ND | $\epsilon$ | Relative stiffness mismatch (incl. electrostatic softening) | ND |
| $f$ | Excitation force | ND | $F$ | Peak value of $f$ | ND |
| $n$ | Random force | ND | $\theta$ | MILO phase-shift | (°) |
| $A_{Duff}$ | Critical Duffing amplitude | ND | $A_{damp}$ | Critical damping amplitude | ND |
| $V_B$ | Bias voltage | (V) | $v_{OUT}$ | Voltage at AFE output | (V) |
| $v_{DRV}$ | Drive voltage | (V) | $v_{drv}$ | Peak value of $v_{DRV}$ | (V) |
| $v_{COMP}$ | Voltage at comparator output | (V) | $C_0$ | Capacitance of resonator | (F) |
| $C_f$ | AFE feedback capacitance | (F) | $R_f$ | AFE feedback resistance | (Ω) |

Table 1 – Main notations used in the paper. A suffixed $x$, resp. $y$, means the value applies only to resonator $x$, resp. $y$ (e.g. $F_x$).

Dropping the the $v_x^2$ and $v_y^2$ terms in (1), and the terms resulting in DC or 2Ω components of the restoring force, we obtain:

$$x\left(1+\kappa-\frac{3}{2}\eta_x-\frac{35}{16}\eta_x x^2\right)+\left(\frac{1}{Q_x}+\alpha_x x^2\right)\frac{dx}{dt}+\frac{d^2x}{dt^2}\approx\frac{2\eta_x}{(1-x)^{\frac{3}{2}}}v_x(t)+n_x(t). \qquad \text{(3-a)}$$

$$y\left(1-\kappa-\frac{3}{2}\eta_y-\frac{35}{16}\eta_y y^2\right)+\left(\frac{1}{Q_y}+\alpha_y y^2\right)\frac{dy}{dt}+\frac{d^2y}{dt^2}\approx\frac{2\eta_y}{(1-y)^{\frac{3}{2}}}v_y(t)+n_y(t). \qquad \text{(3-b)}$$

Note that the resulting model is nearly identical to (A-1), in appendix A, the main difference being the actuation nonlinearity appearing on the right-hand side, which is known to induce waveform-dependent phenomena [12]. This effect is specifically studied in section II-2-b.

### II-1-b Electrostatic tuning of the resonators

The proper operation point of MILOs is when the resonators have zero stiffness mismatch, i.e. when

$$2\kappa - \frac{3}{2}(\eta_x - \eta_y) = 0. \qquad (4)$$

Thus, it is possible to tune the resonators by setting their bias voltages so that (4) is verified. From this operation point, changing the bias voltage of resonator $y$ by a small amount from $V_{By}$ to $V_{By} + \delta V_{By}$, for instance, simulates a relative mechanical stiffness mismatch $\delta\epsilon$ according to:

$$\delta\epsilon = \frac{3}{2}\eta_y \frac{\delta V_{By}}{V_{By}}. \qquad (5)$$

Note that changing the bias voltage of a resonator also changes its Duffing coefficient and the amplitude of its driving force.

Measuring the MILO's oscillation frequency at small oscillation amplitudes for different bias voltages yields the following relation between the electromechanical transduction coefficient and bias voltage

$$\eta_{x,y} \approx \chi \times V_{Bx,y}^2 \qquad (6)$$

with $\chi = 3.35 \times 10^{-6}$. According to (2), this corresponds to a pull-in voltage equal to 235V.

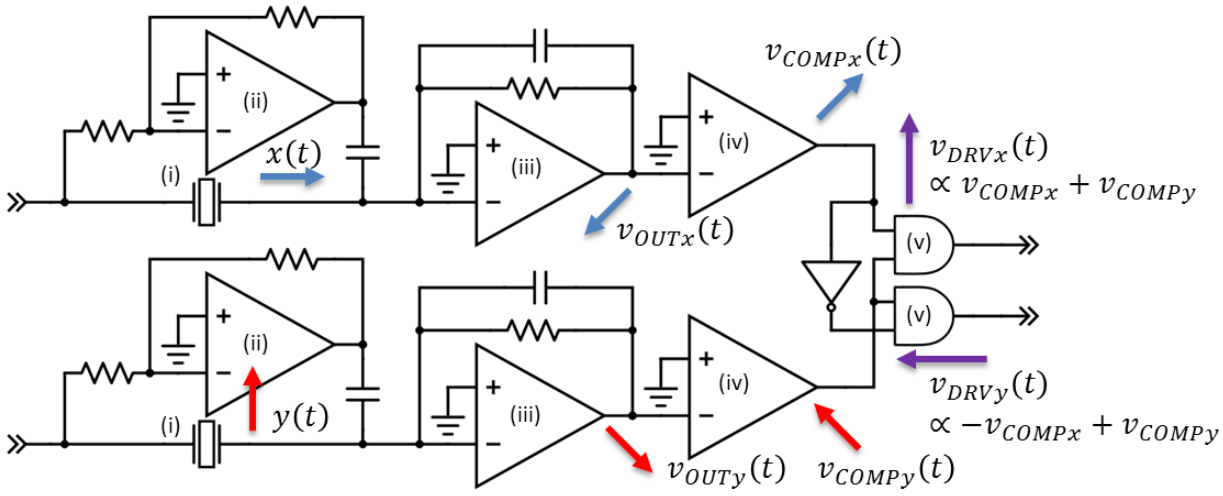


Fig. 3 – Schematic of the studied MILO, consisting of (i) MEMS resonators, (ii) feedthrough compensation stages, (iii) readout stages, (iv) comparators and (v) logic gates. The resistive bridges used for setting drive voltage values have been omitted, and passive bandpass filters at the comparators inputs as well. The arrows correspond to the phasor representation of the signals in the system when $\epsilon = 0$ and $\phi = 90°$. With

$\theta = 45°$, the digital mixer generates actuation voltages (purple arrows) with a 90° phase-lead with respect to the mechanical motion.

## *II-2 Electronic circuit and transduction*

A schematic of the studied MILO is represented in Fig. 3. The angle $\theta = \theta_{det} + \theta_{comp} + \theta_{act}$ is the sum of $\theta_{det}$, the phase-shift resulting from the detection transducer and analog front-end (AFE), $\theta_{comp}$, the phase-shift resulting from the comparator, and $\theta_{act}$ the phase-shift resulting from the driving stage and actuation transducer at the digital mixer output. Angle $\theta$ is an important parameter, since it sets the value of the phase between the resonator motion $(x(t), y(t))$ and the excitation signal $(f_x(t), f_y(t))$ in each loop, which must be 90° for each resonator to be nominally driven at resonance. Setting $\theta = 45°$ guarantees that this is indeed the case, as illustrated in Fig. 3, where $\theta_{det} = -135°$, $\theta_{comp} = 180°$ and $\theta_{act} = 0°$. We first give a general description of this circuit, before focusing on how motional oscillation amplitudes or actuation forces may be derived from the electrical signals.

### II-2-a General description of the oscillator loop

The motional signals are amplified with transimpedance amplifiers, with equal values of the resistive and capacitive part of the feedback impedance at resonance, i.e. $C_f = 15\text{pF}$, $R_f = 160\text{k}\Omega \approx 1/2\pi f_0 C_f$. This results in a 45° phase-lag compared to a regular charge amplifier (with $R_f \gg 1/2\pi f_0 C_f$). The output voltage $v_{OUTx}$ then satisfies

$$\frac{d}{dt}(v_{OUTx}) + v_{OUTx} = -\frac{V_{Bx}}{2}\frac{C_0}{C_f}\frac{dx}{dt} \times \frac{1}{(1-x)^{3/2}}, \quad (7)$$

where $C_0 \approx 0.5\text{pF}$ is the nominal capacitance of the resonator. Note that the capacitance changes as the inverse of the square root of $x$ because of the non-uniform deformation along the length of the beam [15]. Note also that (7) only holds provided capacitive feedthrough is properly cancelled. In our setup, feedthrough cancellation is enforced via an active attenuator stage in parallel with the resonator, as illustrated in Fig. 3. Low-noise, high-speed AD8065 operational amplifiers are used for these two stages.

The binary-valued drive signals $v_{DRVx}$ and $v_{DRVy}$, with peak values $v_{drvx}$ and $v_{drvy}$, are generated through a set of comparators (AD8561), logic gates (74HCT04 and 74HCT08) and potentiometers, as in [7]. Passive bandpass filters are used at the comparator inputs to attenuate unwanted signals below 6kHz or above 600kHz. A small amount of high-frequency hysteresis is also introduced, as proposed in [16]. All in all, simulations and measurements show that the phase delay introduced by the mixer is nearly independent of the amplitude or the harmonicity of its inputs, so that the electronics enforce the condition $\theta = 45°$ regardless of the oscillation amplitude, provided it is significantly higher than a few mV.

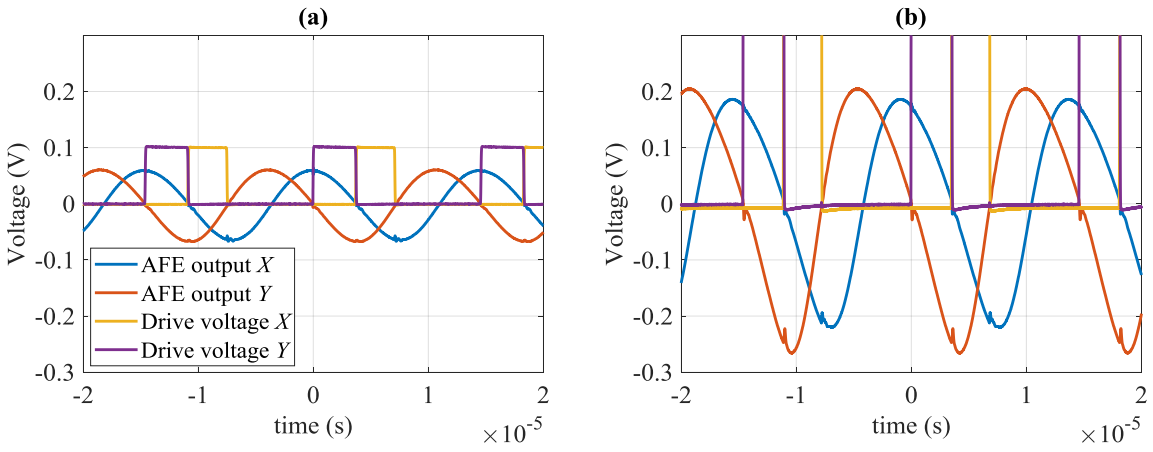


Fig. 4 – Typical waveforms at the AFE outputs and at the resistive bridge outputs when $V_{Bx} = 40\text{V}$, and $V_{By} \approx 36\text{V}$, so that $\phi \approx 90°$, in the cases (a) $v_{drvx} = v_{drvy} = 100\text{mV}$, and (b) $v_{drvx} = v_{drvy} = 1\text{V}$.

Small and large-amplitude waveforms are shown in Fig. 4, highlighting the efficiency of the feedthrough removal, and also the distortion resulting from the detection nonlinearity for large values of motional oscillation amplitudes $X$ and $Y$.

### II-2-b Transduction

From (7), one may determine the relation between the RMS value at the amplifier output, which is measured in our experiments, and the mechanical oscillation amplitude. To this end, the solution of (7) is calculated assuming the input $x(t)$ is harmonic, i.e. $x(t) = X \sin \Omega t$, and approximating the output $v_{OUTx}$ with harmonic balance (20 harmonics are used). Then a simple model is fitted to infer $X$ from the RMS value of $v_{OUTx}$:

$$X = \frac{Z}{1+0.5Z^2}, \quad \text{(8-a)}$$

$$Z = 4\frac{C_f}{C_0}\frac{\text{RMS}(v_{OUTx})}{V_{Bx}}. \quad \text{(8-b)}$$

with 0.8% accuracy up to 50% of the gap. In our setup, the ratio $C_f/C_0$ is measured to be equal to 35.

With the same approach, one may also determine how the amplitude of the actuation force is related to that of the drive voltage. Two opposing effects result in a nearly linear relation between these two quantities. First of all, as a result of detection nonlinearity, $v_{OUTx}$ and $v_{OUTy}$ become distorted at large oscillation amplitudes (see. Fig. 4-b). Consequently, the width of the pulses delivered to the resonators (which depends on when $v_{OUTx}$ and $v_{OUTy}$ change signs) is a monotonically decreasing function of amplitude, going from 24.5% duty-cycle when $X = Y = 0.1$, to 23% when $X = Y = 0.5$. This phenomenon tends to make the drive less efficient at large oscillation amplitudes, since less energy per cycle is injected into the resonators. However, actuation

nonlinearity tends to make electrostatic drive more efficient as the oscillation amplitude increases (ultimately leading to resonant pull-in [15]). Our simulations, which take these two opposing effects into account, show that the relation between the amplitude of the force acting on one resonator and its drive voltage is nearly linear and independent of oscillation amplitude, with a 3.5% worst-case error when $X = Y = 0.5$. One may then neglect these two phenomena altogether and consider, for the purpose of fitting to experimental data, that both resonators are excited by 25% duty-cycle square waves, with peak value:

$$F_{x,y} \approx 2 \times \eta_{x,y} \times \frac{v_{drvx,y}}{V_{Bx,y}}. \qquad (9)$$

## *II-3 Characterization of nonlinear damping*

The presence of nonlinear damping in the resonators used in the present work was observed, but not fully characterized, in [14]. Here, this phenomenon is evidenced by the fact that, between Fig. 4-a and Fig. 4-b, the oscillation amplitude at the amplifier output increases by a factor which is much less than 10, although the drive voltage goes from 100mV to 1V. One may precisely estimate the quadratic damping coefficients of the resonators through the relation between their oscillation amplitude and their excitation force. Indeed, when the resonators oscillate in quadrature, a first-harmonic, steady-state analysis of (3) (see appendix B) yields:

$$X\left(\frac{1}{Q_x} + \frac{1}{4}\alpha_x X^2\right) = F_x\frac{\sqrt{2}}{\pi}, \qquad Y\left(\frac{1}{Q_y} + \frac{1}{4}\alpha_y Y^2\right) = F_y\frac{\sqrt{2}}{\pi} \qquad (10)$$

where $F_x$ and $F_y$ are given by (9).

We represent in Fig. 5 the experimental curves of the $F_x/X$ and $F_y/Y$ ratios obtained with $V_{Bx} = 40V$ and $V_{By} = 36V$, for drive voltages ranging between 50mV and 1V. For each point, the value of the oscillation amplitude is obtained from the measured RMS voltage through (8), and the value of the force is derived from (9). This figure confirms the quadratic dependence of the damping coefficient to the oscillation amplitude. The (inverse of the) quality factor of each resonator is given by the horizontal line.

Repeating this experiment for other values of $V_{Bx}$ and $V_{By}$ shows that quality factors $Q_x$ and $Q_y$ do not depend on bias voltage, but that coefficients $\alpha_x$ and $\alpha_y$ do. This observation is consistent with the hypothesis that, in our MEMS devices, nonlinear damping results from internal resonance, as considered in [14].

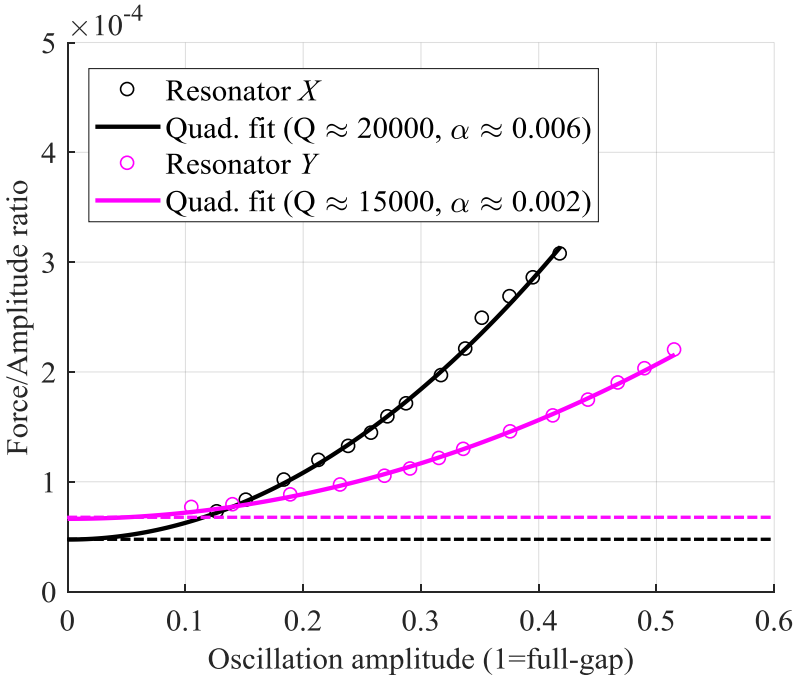


Fig. 5 – Characterization of nonlinear damping. Experimental measurements (circles) and quadratic fits (full lines). The dashed line corresponds to what would be obtained with a linear model of damping.

# III Experimental sensitivity analysis

## *III-1 Experimental protocol*

We are interested in verifying the consistency of the properties established in [10], and summed up in Appendix A, regarding the sensitivity to mismatch and the sensitivity to intrinsic noise of MILOs in the nonlinear regime. In this sub-section, we explain how these quantities may be experimentally assessed.

### III-1-a Sensitivity to mismatch

Sensitivity to mismatch is straightforward to measure. This is done in two steps. First, for a given peak drive voltage $v_{drvx} = v_{drvy}$, and a given value of $V_{Bx}$, one adjusts $V_{By}$ so that the two resonators oscillate in quadrature ($\phi = 90°$) – practically, this condition is obtained by finding the value of $V_{By}$ for which the duty cycle of $v_{DRVx}$ is equal to that of $v_{DRVy}$. The corresponding mechanical oscillation amplitudes ($X$ and $Y$) and amplitude ratio $R = X/Y$ are estimated from the RMS values of $v_{OUTx}$ and $v_{OUTy}$ with (8).

Then, a stiffness variation is induced by changing the value of $V_{By}$ by $\delta V_{By}$ (by an "infinitesimal" amount, about 1% in all of our experiments), with the corresponding change in $\epsilon$ given by (5). The resulting phase difference variation $\delta\phi$ and amplitude variations $\delta X$ and $\delta Y$ are measured.

The sensitivity to mismatch can then be calculated by differentiating the results obtained in the two steps with respect to $\epsilon$. These two steps are repeated for different values of the drive voltage (ranging between 50mV and 1V) and of the bias voltage $V_{Bx}$ (from 25V to 40V).

### III-1-b Sensitivity to noise

Sensitivity to noise is more tricky to determine. However, this quantity may be assessed by purely deterministic means. In our first harmonic analysis, the effect of thermomechanical noise in the system amounts to four independent force components ($n_{cosx}, n_{cosy}, n_{sinx}, n_{siny}$) acting on the resonators (see appendices A and B). In particular, from (B-2), we see that a quasi-static variation $\delta F_y$ of $F_y$ has the same impact on amplitude ratio $R$ as $n_{cosy}$, and we find:

$$\left|\frac{\partial R}{\partial F_y}\right| = \frac{1}{\pi}\left|\frac{\partial R}{\partial n}\right|. \quad (11)$$

Furthermore, for large oscillation amplitudes (with respect to either $A_{Duff}$ or $A_{damp}$), we also have

$$\left|\frac{\partial \phi}{\partial F_y}\right| = \frac{1}{\pi}\left|\frac{\partial \phi}{\partial n}\right|. \quad (12)$$

Hence, the sensitivity to noise may be determined in a two-step process, as above, but this time the second step consists in changing the value of $v_{drvy}$ by a small amount $\delta v_{drvy}$ (from 20mV to 50mV, as $v_{drvy}$ changes from 100mV to 1V), with the corresponding change in driving force given by (9)

$$\delta F_y = 2 \times \eta_y \times \frac{\delta v_{drvy}}{V_{By}}. \quad (13)$$

### III-1-c Model comparison

All the model parameters are summed up in table 2.

| Parameter | $C_f/C_0$ | $\chi$ | $Q$ | $\alpha$ | |
|---|---|---|---|---|---|
| Unit | no dim. | $V^{-2}$ | no dim. | no dim. | |
| Condition | | | | $V_{Bx} = 25V$ | $V_{Bx} = 40V$ |
| Resonator $x$ | 32.5 | $3.35 \times 10^{-6}$ | $19.5 \times 10^3$ | $11.7 \times 10^{-3}$ | $6.68 \times 10^{-3}$ |
| Resonator $y$ | | | $14.4 \times 10^3$ | $1.73 \times 10^{-3}$ | $2.66 \times 10^{-3}$ |

Table 2 – Numerical values of model parameters.

Except for $C_f/C_0$, all the parameters are obtained by characterizing the resonators, as explained in section II: the value of $\chi$ is obtained by measuring the electrostatically-induced frequency shift, while damping related parameters are obtained by fitting parabolas to the $F_x/X$ vs. $X$ and $F_y/Y$ vs. $Y$ curves. Note that this last step requires $C_f/C_0$ to be known. The values of $Q_{x,y}$ and $\alpha_{x,y}$ given in table 1 are those obtained for $C_f/C_0 = 32.5$. This value of 32.5 is within component tolerances of the nominal value (equal to 30) of $C_f/C_0$, and gives a slightly better fit between the model and the experimental results, as shown in the following sections.

### *III-2 Results*

Experimental results obtained with the protocol described in the previous section are shown in Fig. 6. The results obtained with a quasi-static model of the fluctuations (continuous lines) are superposed to the experimental data (crosses and circles). In order to improve the readability of this experimental sensitivity analysis, the sensitivities to noise and to mismatch are represented versus the average oscillation amplitude $A_{avg} = (X + Y)/2$.

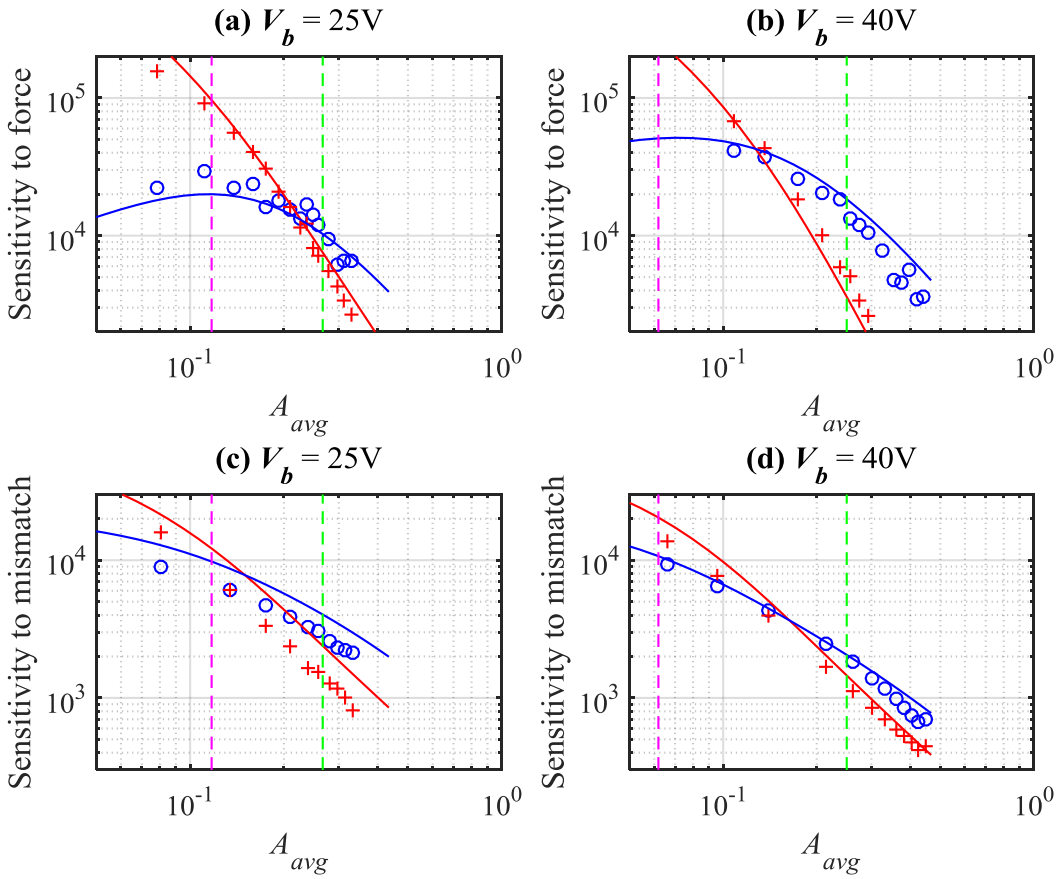


Fig. 6 – Experimental (circles and crosses) and simulated (full lines) sensitivities of the MILO with different operating conditions. Blue corresponds to phase difference, red to amplitude ratio. Vertical dashed lines correspond to the average critical Duffing (magenta) and damping (green) amplitudes of the resonators.

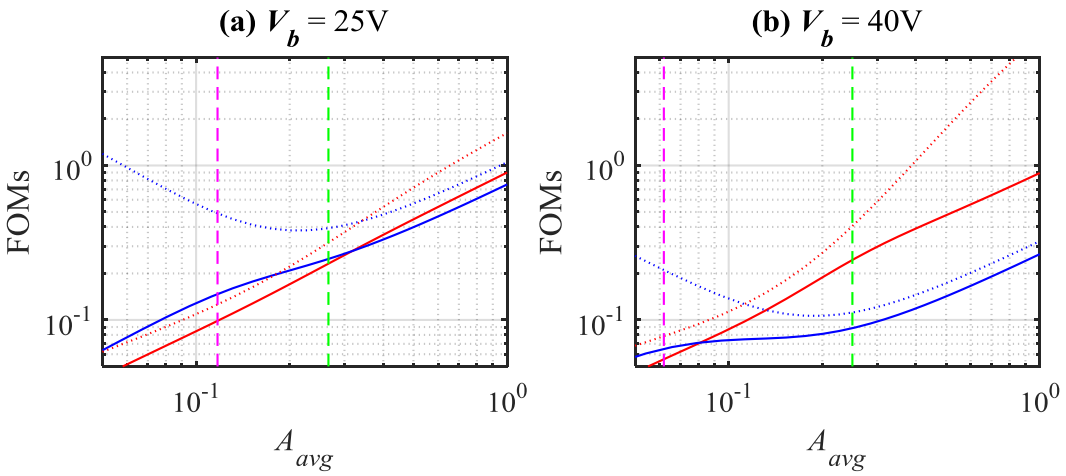


Fig. 7 – Extrapolated FOM of amplitude ratio (red) and of phase difference (blue), for $V_{Bx} = 25V$ (a) and $V_{Bx} = 40V$ (b) vs. oscillation amplitude. Vertical dashed lines correspond to the average critical Duffing (magenta) and damping (green) amplitudes of the resonators. The dotted lines represent the ratio of sensitivity to mismatch over sensitivity to force.

We can verify that there is a very good fit between the model and the experimental data. There is a quantitative fit for most curves over several orders of magnitude, except in the case of sensitivity to mismatch at $V_{Bx} = 25V$, where the model systematically overestimates sensitivity by about 3dB. However, even in that case, the experimental and simulated results have highly similar trends. Thereby, the theoretical analysis of [10] is validated.

The two sets of results are qualitatively different in the sense that, in the case $V_{Bx} = 25V$ (and $V_{By} \approx 17V$), the average critical Duffing amplitude is about twice as large as in the case $V_{Bx} = 40V$ (and $V_{By} \approx 36V$) - 11% of the gap, as opposed to 6% of the gap. On the other hand, the critical damping amplitude is relatively unchanged - 28% of the gap in the first case, and 26% in the second. Thus, in the case $V_{Bx} = 40V$, there is a wider region in which nonlinear stiffening dominates, in which the sensitivity to force (and hence to intrinsic noise) of the phase-difference decreases at a much slower rate than its sensitivity to mismatch. In the same region, the sensitivity to force of the amplitude ratio decreases with $A_{avg}$ much faster than that of the phase difference. Since the sensitivities to mismatch of these two quantities decrease at approximately the same rate, the FOMs of the different output metrics (extrapolated from our model) are quite different, depending on whether $V_{Bx} = 25$V or $V_{Bx} = 40$V, as shown in Fig. 7.

Systematic errors may result from our overlooking the dependence on bias voltage of a system parameter: for example, the static deformation of the resonator beam (and consequently $C_f/C_0$), which is bias voltage-dependent, is not accounted for. Moreover the expressions of the electrostatic force used in (1) and that of the motional current used in (7) are valid in the case of an initially straight clamped-clamped beam oscillating

along its first eigenmode [15], whereas, in the present case, the beam has a pressure-induced initial deformation, which also influences the electrostatic softening coefficient. However, we do not have sufficient data to accurately account for these effects and must content ourselves with the current model. Measurement errors are of a different nature depending on whether the oscillation amplitude is small or large (the amplitude span of our experiment is from 0.05% to 50% of the gap): at small amplitudes, the sensitivity to mismatch is large (on the order of $14 \times 10^3$), making it difficult to manually tune $V_{By}$ to obtain $\phi = 90°$. Furthermore, the sensitivity to driving force fluctuations (and more generally to noise) is also large, which results in unstable readings. At large amplitudes, both sensitivities are considerably reduced (by about one order of magnitude, concerning the sensitivity to mismatch), and are therefore more difficult to estimate because of the limited accuracy of the oscilloscope (MSO5204) used in these experiments.

# IV Spectral analysis

In this section, we seek to validate the results established in [10] regarding the dynamic behavior of WCRs, through an analysis of the spectra of different output metrics.

## *IV-1 Experimental protocol*

The spectra presented in this section are obtained by setting $V_{Bx} = 40V$, and $V_{By} \approx 36V$ so that the resonators oscillate in quadrature. Then 50 consecutive 4-second-long acquisitions of $v_{OUTx}$ and $v_{OUTy}$ are taken with a high-resolution 2-channel digitizer (Alazar ATS660, 16-bit digitizer) at a sampling frequency of 500 kHz. For each acquisition, $v_{OUTx}^2$, $v_{OUTy}^2$ and $v_{OUTx} \times v_{OUTy}$ are averaged with a sliding window, yielding an estimate of the fluctuations of $R$ and $\phi$ over time. Reduced-variance spectra are then obtained by averaging the 50 periodograms resulting from each acquisition (Bartlett's method).

## *IV-2 Results*

The power spectra of the fluctuations of $R$ and $\phi$ obtained at three oscillation amplitudes ($A_{avg}$ varying from 0.26 to 0.46) are represented in Fig. 8-a and Fig. 8-b. The measured noise levels are much larger than the thermomechanical noise floor or than our digitizer's. They are consistent with the voltage fluctuations of the power supplies, which result, through $V_{Bx}$ and $V_{By}$, in additive measurement noise at the AFE outputs, and in a slow drift of $\epsilon$ around 0. More precisely, assuming $V_{Bx}(t) = \overline{V_{Bx}} + \delta V_{Bx}(t)$, equation (7) becomes:

$$\frac{d}{dt}(v_{OUTx}) + v_{OUTx} \approx -\frac{\overline{V_{Bx}}}{2}\frac{C_0}{C_f}\frac{dx}{dt} \times \frac{1}{(1-x)^{\frac{3}{2}}} - \frac{C_0}{C_f}\frac{d\delta V_{Bx}}{dt}, \qquad (14)$$

and (4-5) yield:

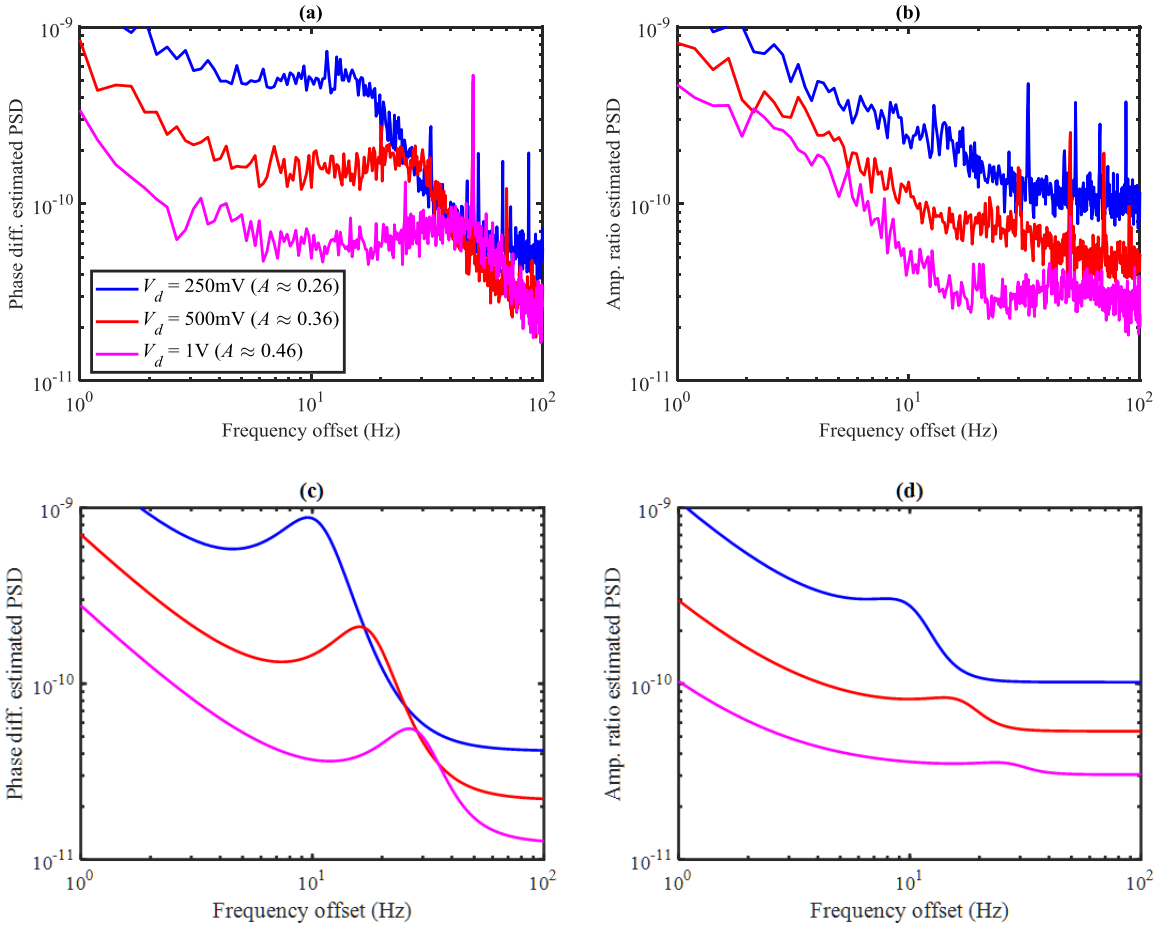


Fig. 8 – Experimental phase difference (a) and amplitude ratio (b) spectra, at three different drive amplitudes. Simulated spectra of phase difference (c) and amplitude ratio (d) accounting for bias voltage noise.

$$\delta\epsilon(t) \approx -\frac{3}{2}\chi\overline{V_{Bx}} \times \delta V_{Bx}(t). \quad (15)$$

The superposition of these two effects can partly explain the measured spectra: measurement noise results in a white noise floor, while the signal transfer function (STF) of the output metrics – equations (36-38) in [10] – amplifies the variations of $\epsilon$ around 0. The simulated spectra accounting for bias voltage fluctuations are shown in Fig. 8-c and 8-d.

We find a rather good agreement between the experimental and simulated spectra of $R$. The level of the measured fluctuations corresponds to what is theoretically predicted when accounting only for bias voltage fluctuations. The same characteristic bump is found near the cutoff frequency, although it is a little less marked in the experimental spectra, and the value of the cutoff frequency increases with oscillation amplitude in the same proportions. At very low frequency offset, the experimental spectrum of $R$ is dominated by flicker noise: this is only partly explained by bias voltage drift, which suggests that another phenomenon, such as intrinsic mechanical stiffness fluctuations [17] or quality factor fluctuations, may be at work.

The comparison of the experimental and simulated spectra of $\phi$ is more puzzling, in the sense that the resonance peak marking the cutoff frequency is much less marked in the experimental spectra than in theory. However, this may be a consequence of fluctuations of the cutoff frequency (resulting from the bias-voltage dependence of some of the system parameters, for example) over the time required for doing the 50 measurements. These fluctuations can probably not be considered infinitesimal (and may not fall into the framework of analysis of [10]), which may explain the spread-out peak in the spectrum of $\phi$. Finally, it is interesting to note that there is a quantitative fit between theory and experiment as far as flicker is concerned: thus, one can probably rule out mechanical stiffness fluctuations (which would affect equally both $R$ and $\phi$) as the cause of the low frequency fluctuations of $R$.

## *IV-3 Input-referred noise*

One may calculate the spectrum of the input-referred noise for a given output-metric by dividing the estimated spectrum of its fluctuations (Fig. 8-c for $\phi$, Fig. 8-d for $R$) by its signal transfer function $STF_\phi$ or $STF_R$ (B-3). The results are shown in Fig. 9. Regardless of the oscillation amplitude, input-referred noise is always smaller for $\phi$ than for $R$. To determine whether nonlinear operation is interesting or not in the context of a given application, one may determine the power of input-referred noise over a given frequency bandwidth. For example, if we consider the [0,100Hz] bandwidth, we can see from Fig. 9 that there would indeed be a great interest in nonlinear operation, in particular for the amplitude ratio output metric: the power of input-referred noise is divided by 15 for $R$, and by 4 for $\phi$, as $v_{drv}$ goes from 250mV to 1V. On the other hand, if we consider the [0,10Hz] bandwidth, then nonlinear operation only makes things worse: the power of input-referred noise is then multiplied by 4 for $R$, and by 1.1 for $\phi$, as $v_{drv}$ goes from 250mV to 1V.

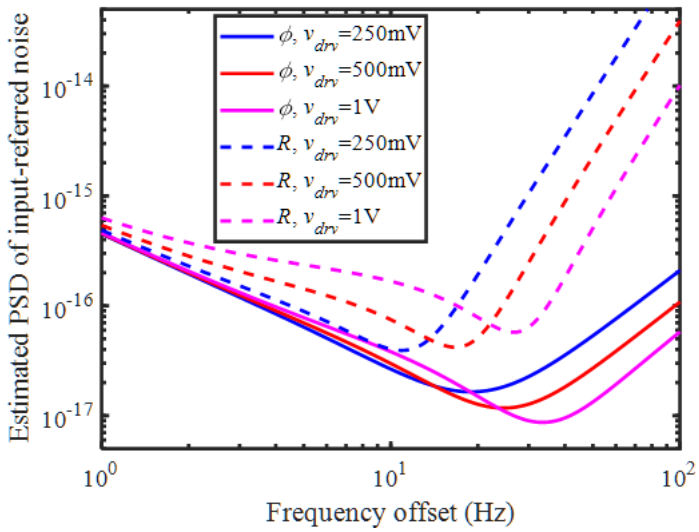


Fig. 9 – Input-referred noise (fluctuations of $\epsilon$) estimated from the spectra of Fig. 8-c and 8-d.

# V Conclusion

This paper provides, for the first time, an experimental proof of several results postulated in [10] for nonlinear WCRs with a critical Duffing amplitude smaller than the critical damping amplitude ($A_{Duff} < A_{damp}$). Using two matched resonators displaying such nonlinear behavior, we have verified:

- the similar decrease in parametric sensitivity of $R$ and $\phi$ in WCRs operated above $A_{Duff}$.
- the improved robustness to drive-level fluctuations (and hence to intrinsic oscillator noise) of $R$ between $A_{Duff}$ and $A_{damp}$.
- the amplitude-dependence of the bandwidth in which $R$ and $\phi$ are sensitive to intrinsic noise and to stiffness mismatch $\epsilon$.

These experimental results were found to be in quantitative agreement with our simulations, which validates the analysis in [10].

As mentioned in section I, sensor performance was not our primary concern. Still, the results presented in this paper may be analyzed in this respect. We have shown that, in the current setup, operating at a large oscillation amplitude results in a wider bandwidth for both $R$ and $\phi$, and that the input-referred noise of both output metrics decreased with oscillation amplitude over a 100Hz bandwidth, but increased over a 10Hz bandwidth. Our calculations also showed $\phi$ to have smaller input-referred noise than $R$. However, this should not be considered a definitive or a general result, but is probably quite specific to our resonators, with predominant damping nonlinearity, and to our circuit and instrumentation setup, with bias voltage fluctuations shadowing all other noises in the system.

Finally, several questions remain unanswered, and require further investigation. First, the spread-out outlook of the peaks in the observed experimental spectra is unexplained, although some hypotheses were formulated as to this phenomenon. One may then refine the models in [10] to account for flicker, drift and finite fluctuations of the system parameters, for example by using a non-perturbed model such as (7) in [10] or multiple-scale analysis [18]. More practically, one may also try to reproduce the experiments in a carefully controlled environment, or with better-matched resonators (which would more efficiently reject common-mode variations).

Another point that requires further study is the behavior of WCRs when damping nonlinearity dominates: first, as mentioned in [10], there does not seem to be a definitive theory linking thermomechanical noise to nonlinear damping. Decreasing (bias voltage) noise in our setup may then help us investigate this phenomenon. Alternatively, other resonators with increased damping, in particular MEMS resonators operated in ambient atmospheric pressure and subject to squeezed-film damping, may be better suited to this investigation.

# References


[1] C. Zhao et al., “A review on coupled MEMS resonators for sensing applications utilizing mode localization”, Sensors and Actuators A, vol. 249, pp. 93-111, 2016.

[2] M. Pandit, C. Zhao, G. Sobreviela, A. A Seshia, “Immunity to Temperature Fluctuations in Weakly Coupled MEMS Resonators”, 2018 IEEE Sensors Conference, pp. 1-4, 2018.

[3] J. Juillard, P. Prache, N. Barniol, “Analysis of mutually injection-locked oscillators for differential resonant sensing”, IEEE Transactions on Circuits and Systems 1, vol. 63, pp. 1055-1066, 2016.

[4] P. Prache, J. Juillard, P. Maris Ferreira, N. Barniol, M. Riverola, “Design and characterization of a monolithic CMOS-MEMS mutually injection-locked oscillator for differential resonant sensing”, Sensors and Actuators A, vol. 269, pp. 160-170, 2018.

[5] P. Thiruvenkatanathan, J. Yan, J. Woodhouse, A. A. Seshia, “Enhancing parametric sensitivity in electrically coupled MEMS resonators”, IEEE Journal of Microelectromechanical Systems, vol. 18, pp. 1077-1086, 2009.

[6] J. Juillard ; P. Prache, P. M. Ferreira, N. Barniol, “Ultimate Limits of Differential Resonant MEMS Sensors Based on Two Coupled Linear Resonators”, IEEE Transactions on Ultrasonics, Ferroelectrics, and Frequency Control, vol. 65, pp. 2440-2448, 2018.

[7] J. Juillard, A. Mostafa, P. M. Ferreira, “Nonlinear enhancement of locking range of mutually injection-locked oscillators for resonant sensing applications”, European Frequency and Time Forum, pp. 109-113, 2018.

[8] J. Juillard, A. Mostafa, P. M. Ferreira, “Analysis of resonant sensors based on mutually injection-locked oscillators beyond the critical Duffing amplitude”, European Frequency and Time Forum, pp. 114-118, 2018.

[9] M. Pandit et al., “Reduction of Amplitude Ratio Dependence on Drive Level in Mode Localized Resonant MEMS Sensors”, IEEE Sensors conference, 3 pp., 2017.

[10] J. Juillard, A. Mostafa, P. M. Ferreira, “Nonlinear operation of resonant sensors based on weakly-coupled resonators: theory and modeling”, available as preprint on HAL, 2019.

[11] J. Mandle, O. Lefort, A. Migeon, “A new micromachined silicon high accuracy pressure sensor”, Sensors and Actuators A, vol. 46-47, pp.129-132, 1995.

[12] A. Brenes, J. Juillard, L. Bourgois, F. Vinci dos Santos, “Influence of the Driving Waveform on the Open-Loop Frequency Response of MEMS Resonators With Nonlinear Actuation Schemes”, IEEE/ASME Journal of Microelectromechanical Systems, vol. 25, pp. 812-820, 2015.

[13] A. Brenes, “Modélisation des phénomènes non-linéaires dans un capteur MEMS résonant pour l'optimisation de ses performances et de sa fiabilité,” Ph.D. thesis, Université Paris-Saclay, 2015.

[14] A. Brenes, J. Juillard, F. Vinci dos Santos, “Electrostatically-induced modal crosstalk phenomena in resonant MEMS sensors”, Symposium on Design, Test, Integration and Packaging of MEMS MOEMS, pp. 1-4, 2014.

[15] J. Juillard, “Analysis of resonant pull-in of microelectromechanical oscillators”, Journal of Sound and Vibration, vol. 350, pp. 123-139, 2015.

[16] AD8561 Datasheet, rev. D, https://www.analog.com/media/en/technical-documentation/data-sheets/AD8561.pdf

[17] M. Sansa et al., “Frequency fluctuations in silicon nanoresonators”, Nature Nanotechnology, vol. 11, pp. 552-558, 2016.

[18] A. H. Nayfeh, D. T. Mook, “Nonlinear Oscillations”, Wiley, 1979.

# Appendix A

Here the main results from [10] are summed up, in the case of two nominally-identical resonators governed by the (non-dimensionalized) equations:

$$(1+\epsilon+\gamma_x x^2)x+\left(\frac{1}{Q_x}+\alpha_x x^2\right)\frac{dx}{dt}+\frac{d^2x}{dt^2}=f_x\left(x,\frac{dx}{dt},y,\frac{dy}{dt}\right)+n_x(t), \text{ (A-1-a)}$$

$$\left(1-\epsilon+\gamma_y y^2\right)y+\left(\frac{1}{Q_y}+\alpha_y y^2\right)\frac{dy}{dt}+\frac{d^2y}{dt^2}=f_y\left(x,\frac{dx}{dt},y,\frac{dy}{dt}\right)+n_y(t), \text{ (A-1-b)}$$

where $t$ is time, $x$ and $y$ are the motional signals, with amplitudes $X$ and $Y$ and phase difference $\phi$, $f_x$ and $f_y$ are the forces used for driving the resonators and coupling them, $n_x$ and $n_y$ are independent random forces typically resulting from thermomechanical fluctuations (“intrinsic” noise sources), $Q_{x,y}$ are the resonators’ quality factors, $\gamma_{x,y}$ are nonlinear (Duffing) stiffness coefficients, $\alpha_{x,y} \geq 0$ are nonlinear damping coefficients and $\epsilon$ is (half) the relative stiffness mismatch one seeks to measure. It is shown in [10] that the properties of passively- or actively-coupled resonators are highly amplitude-dependent. In the case of mutually injection-locked oscillators (MILOs), most relevant to the present paper, important “cutoff” amplitudes are the critical Duffing amplitude, defined as

$$A_{Duff}=\sqrt{\frac{2}{3|\gamma|Q}}, \qquad \text{(A-2)}$$

and the critical damping amplitude as:

$$A_{damp}=\frac{2}{\sqrt{\alpha Q}} \text{ (A-3)}$$

when $Q_{x,y} = Q$, $\alpha_{x,y} = \alpha$, $\gamma_{x,y} = \gamma$. The expressions of these threshold amplitudes in the case of mode-localized oscillators (MOLOs) are obtained by substituting $|\kappa|$ for $1/Q$ in (A-2) and (A-3), where $\kappa$ is the (non-dimensional) coupling stiffness of the resonators. With these definitions in mind, assuming the two resonators nominally oscillate at the same amplitude $X = Y = A$ when $\epsilon = 0$, the following properties hold:

- if $A \gg A_{Duff}$ or $A \gg A_{damp}$, the parametric sensitivity to relative stiffness mismatch $\epsilon$ of the amplitude ratio $R = X/Y$ and of the phase difference $\phi$ - only relevant for MILOs - decrease as $1/A^2$.
- if $A_{damp} \gg A \gg A_{Duff}$ (dominant stiffness nonlinearity), at most one oscillation state is stable, depending on the sign of the Duffing parameter $\gamma$, and on another system parameter: feedback phase $\theta$ in the case of MILOs, coupling stiffness $\kappa$ in the case of MOLOs operating near the veering zone. Furthermore,
    - the sensitivity to intrinsic noise of $R$ decreases as $1/A^3$.
    - the sensitivity to intrinsic noise of $\phi$ decreases as $1/A$.
- if $A \gg A_{damp}$ (dominant damping nonlinearity), the sensitivity to intrinsic noise of $\phi$ decreases as $1/A^3$.

These properties are limited to a finite bandwidth of quasi-static fluctuations, and an equally finite range of values of $\epsilon$ close to $\epsilon = 0$. They are valid for MILOs and MOLOs indifferently, the only difference being the definition of the threshold amplitudes.

# Appendix B

In the case of a system governed by (A-1), in which coupling is enforced through a digital MILO architecture (Fig. 1) with $\theta = 45°$, the slow dynamics of amplitudes $X(t)$, $Y(t)$ and phase difference $\phi(t)$ are governed by:

$$\dot{X} = -\left(\frac{1}{Q_x} + \frac{1}{4}\alpha_x X^2\right)\frac{X}{2} + \frac{1}{2}\left(\frac{F_x}{\pi}\left(\frac{\sqrt{2}}{2} + \sin\left(\frac{\pi}{4} + \phi\right)\right) + n_{cosx}\right) \qquad \text{(B-1-a)}$$

$$\dot{Y} = -\left(\frac{1}{Q_y} + \frac{1}{4}\alpha_y Y^2\right)\frac{Y}{2} + \frac{1}{2}\left(\frac{F_y}{\pi}\left(\frac{\sqrt{2}}{2} - \sin\left(\frac{\pi}{4} - \phi\right)\right) + n_{cosy}\right) \qquad \text{(B-1-b)}$$

$$\dot{\phi} = -\left(\epsilon + \frac{3}{8}\gamma_x X^2 - \frac{3}{8}\gamma_y Y^2\right) + \frac{1}{2X}\left(\frac{F_x}{\pi}\left(\frac{\sqrt{2}}{2} + \cos\left(\frac{\pi}{4} + \phi\right)\right) + n_{sinx}\right) - \frac{1}{2Y}\left(\frac{F_y}{\pi}\left(\frac{\sqrt{2}}{2} - \cos\left(\frac{\pi}{4} - \phi\right)\right) + n_{siny}\right) \qquad \text{(B-1-b)}$$

where a dot denotes differentiation with respect to time, $F_{x,y}$ are the peak values of the binary valued force delivered to the resonators, and $n_{cosx,y}$, $n_{sinx,y}$ are quadrature and in-phase random fluctuations. The steady-state values of $X$, $Y$ and $\phi$ are found by solving (B-1) after cancelling out the time-derivatives terms on the left-hand side and the random fluctuations. In the simplest case when $Q_{x,y} = Q$, $\alpha_{x,y} = \alpha$, $\gamma_{x,y} = \gamma$, $F_{x,y} = F$ and

$\epsilon = 0$, the steady-state verifies $X = Y = A$ and $\phi = 90°$. Perturbation of (B-1) around this steady-state yields

$$\frac{\dot{\delta X}}{A} = -\frac{1}{2}\left(\frac{1}{Q} + \frac{3}{4}\alpha A^2\right)\frac{\delta X}{A} - \frac{1}{4}\left(\frac{1}{Q} + \frac{1}{4}\alpha A^2\right)\delta\phi + \frac{1}{2A}\left(n_{cosx} + \frac{\sqrt{2}}{\pi}\delta F_x\right) \qquad \text{(B-2-a)}$$

$$\frac{\dot{\delta Y}}{Y} = -\frac{1}{2}\left(\frac{1}{Q} + \frac{3}{4}\alpha A^2\right)\frac{\delta Y}{A} + \frac{1}{4}\left(\frac{1}{Q} + \frac{1}{4}\alpha A^2\right)\delta\phi + \frac{1}{2A}\left(n_{cosy} + \frac{\sqrt{2}}{\pi}\delta F_y\right) \qquad \text{(B-2-b)}$$

$$\dot{\delta\phi} = -\frac{3}{4}\gamma A^2\left(\frac{\delta X}{A} - \frac{\delta Y}{A}\right) - \frac{1}{2}\left(\frac{1}{Q} + \frac{1}{4}\alpha A^2\right)\delta\phi - \delta\epsilon + \frac{1}{2A}\left(n_{sinx} - n_{siny}\right) \qquad \text{(B-2-c)}$$

where prefix $\delta$ denotes an infinitesimal perturbation of the system's state and of parameters $\epsilon$ and $F_{x,y}$. The transfer functions between fluctuating parameters or noise and phase $\delta\phi$ or amplitude ratio $\delta R = (\delta X - \delta Y)/A$ are straightforward to derive from this set of linear ordinary differential equations, and quasistatic fluctuations of the system's state are obtained by dropping time derivatives from (B-2) altogether. In particular, the expressions of the signal transfer functions between fluctuations of $\epsilon$ and output metrics $R$ or $\phi$ are:

$$STF_R(p) = \frac{\frac{1}{2}\left(\frac{1}{Q}+\frac{1}{4}\alpha A^2\right)}{p^2+\left(\frac{1}{Q}+\frac{1}{2}\alpha A^2\right)p+\frac{1}{2}\left(\frac{1}{Q}+\frac{1}{4}\alpha A^2\right)\left(\frac{1}{2}\left(\frac{1}{Q}+\frac{3}{4}\alpha A^2\right)-\frac{3}{4}\gamma A^2\right)}, \qquad \text{(B-3-a)}$$

$$STF_\phi(p) = -\frac{p+\frac{1}{2}\left(\frac{1}{Q}+\frac{3}{4}\alpha A^2\right)}{p^2+\left(\frac{1}{Q}+\frac{1}{2}\alpha A^2\right)p+\frac{1}{2}\left(\frac{1}{Q}+\frac{1}{4}\alpha A^2\right)\left(\frac{1}{2}\left(\frac{1}{Q}+\frac{3}{4}\alpha A^2\right)-\frac{3}{4}\gamma A^2\right)}. \qquad \text{(B-3-b)}$$